Microstructures and mechanical properties of α-SiC ceramics after high-temperature laser shock peening

Fei Wang[1], Xin Chen[1], Daniel P. DeLellis[2], Amanda R. Krause[2], Yongfeng Lu[3], Bai Cui [1,4,*]

[1]*Department of Mechanical & Materials Engineering, University of Nebraska–Lincoln, Lincoln, NE 68588, USA*

[2]*Materials Science and Engineering Department, University of Florida, Gainesville, FL 32611, USA*

[3]*Department of Electrical and Computer Engineering, University of Nebraska–Lincoln, Lincoln, NE 68588, USA*

[4]*Nebraska Center for Materials and Nanoscience, University of Nebraska–Lincoln, Lincoln, NE, 68588, USA*

*Corresponding author. Tel.: +1 (402) 472-5740; fax: +1 (402) 472 1465; email: bcui3@unl.edu.

Abstract

A novel high-temperature laser shock peening (HT-LSP) process was applied to polycrystalline α-SiC to improve the mechanical performance. HT-LSP prevents microcrack formation on the surface while induces plastic deformation in the form of dislocation slip on the basal planes, which may be caused by the combination of a high shock pressure and a lower critical resolved shear stress at 1000 ℃. A maximum compressive residual stress of 650 MPa, measured with Raman spectroscopy, was introduced into the surface of α-SiC by HT-LSP, which can increase the nanohardness and in-plane fracture toughness of α-SiC by 8% and 36%, respectively. This work presents a fundamental base for the promising applications of HT-LSP to brittle ceramics to increase their plasticity and mechanical properties.

Keywords: Silicon carbide; laser shock peening; residual stress; microstructures; mechanical properties.

1. Introduction

α-SiC is a superior ceramic material that has a wide range of critical applications, such as semiconductor electronic devices that operate at high temperatures or voltages [1], hot sections of jet engines [2], and automobile brake discs [3]. However, similar to other ceramic materials, the application of α-SiC is limited by its low fracture toughness (2.5-3 MPa-$m^{1/2}$) [4]. Thus, it will be beneficial to develop a process that can improve the fracture toughness of α-SiC, as well as other ceramic materials. Laser shock peening (LSP), or laser shock processing, is a surface treatment technique that uses lasers with a nanosecond pulse duration to irradiate a material [5–7]. Rapid expansion of the laser-induced plasma generates a high magnitude of shock waves that can penetrate into the bulk material to a depth of more than 1 mm [8, 9]. The shock wave pressure is sufficiently high (several to tens of GPa) to introduce plastic deformation-induced compressive residual stress[7]. LSP has been successfully applied to improve the stress corrosion cracking resistance, hardness, and fatigue resistance of metallic materials such as stainless steels or aluminum alloys [10–15] . In these applications, the beneficial effects of LSP are generally attributed to the compressive residual stress and deformation-induced hardening [16].

LSP of ceramics is innovative yet challenging due to the intrinsic brittleness of ceramics. As a result, the laser-driven shock waves can result in damage on the surfaces. LSP of ceramic materials, including LSP of α-SiC [16, 17], Al_2O_3 [7, 18], and Si_3N_4 [19], has been reported in the literature and shows promise for improving the mechanical properties of ceramics. For example, LSP was reported to improve the bending strength of Si_3N_4 by 10% [19], enhance the fracture toughness of α-Al_2O_3 by 29% [6 7], and increase the bending strength of α-SiC by 17% [17]. The strength and toughness of these ceramics are improved due to the compressive residual stress induced by LSP. The basic mechanisms are that the compressive residual stress can reduces the effective stress intensity factor at the crack tip, and also offset a part of the applied tensile stress in the bending test thus raising the stress threshold for crack initiation. [17]

It is important to note that in the conventional LSP process, samples remain at room temperature because a sacrificial coating (black vinyl tape or Al foils) protects the samples from laser ablation

damage while deionized water or glass is usually used as the plasma-confining media that mimimize the laser heating effect [20–22]. However, the low dislocation activity, high critical resolved shear stress, and brittleness of ceramics poses technical difficulties for the LSP process at room temperature. For example, Wang *et al.* reported that the LSP treatment at room temperature can generate microcracks in α-Al_2O_3, which can be detrimental to the mechanical properties [7]. To address this problem, a post-annealing heat treatment at 1100-1300 °C was conducted after LSP, which could stabilize the compressive residual stess, heal the microcracks, and thus improve the cracking resistance of α-Al_2O_3 to mechanical impact [23].

Response of α-SiC to mechanical testing is almost purely elastic at room temperature because fracture occurs before yielding. Dislocations in α-SiC have low mobility at temperatures below 800 ºC [24]. LSP of α-SiC at room temperature requires careful control of the laser pulse energy to miminze the microcrack formation [25]. To overcome this technical challenge, a novel high temperature laser shock peening (HT-LSP) technique was developed by our group [26]. The concept of HT-LSP is based on the fact that the slip systems in ceramics are easier to activate at high temperatures than at room temperature. As a result, a high-temperature environment can enhance the plasticity of ceramics and possibly prevent microcrack formation by shock waves during the HT-LSP process. HT-LSP applied to single crystal Al_2O_3 (sapphire) enabled LSP at temperatures higher than 1000 ºC for the first time [27]. The experimental results suggest that HT-LSP at 1200 ºC can minimize the shock wave damage in sapphire while improving the hardness and fracture toughness by 9% and 29%, respectively [27].

This study investigates the influence and fundamental mechanisms of HT-LSP on polycrystalline ceramics using α-SiC as a model material. The microstructural changes caused by HT-LSP were characterized using scanning electron microscopy (SEM) and transmission electron microscopy (TEM). The residual stress distribution on the surface was measured by Raman spectroscopy. The effect of HT-LSP on the local mechanical properties of α-SiC was evaluated by the Vickers indentation method.

2. Experimental procedure

Commercially available silicon carbide (α-SiC) plates were purchased from Ortech Advanced Ceramics (Sacramento, CA). The samples are polycrystalline α-SiC (6H-SiC) fabricated by

pressureless sintering, which were cut to 10×10×2 mm^3 and the surface was polished with diamond lapping films to a mirror finish. X-ray diffraction (XRD) of the α-SiC samples was acquired by using a X-ray diffractometer (SmartLab, Rigaku) with a Cu X-ray tube and operation conditions of 40 kV and 44 mA. XRD pattern was collected over the 2θ range of 20–80° with a step size 0.04° and a dwell time of 0.5 s at each step.

Figure 1 shows the SEM image and XRD pattern of an α-SiC sample before HT-LSP. The α-SiC sample without HT-LSP (Figure 1a) showed a smooth surface after mechanical polishing. The backscattered electron micrograph in Figure 1a reveals that the α-SiC sample contained secondary phases that were further evaluated with EDS. EBSD, and XRD. EDS analysis found the α-SiC sample comprises 3.5 vol.% TiB_2 (white contrast grains) and 3.0 vol.% carbon (dark grains). TiB_2 and carbon (in the form of graphite) were impurities from the powder processing method during the pressureless sintering of α-SiC ceramics [28]. The average grain size of α-SiC was measured to be 6.4±1.5 μm by the EBSD analysis (Figure 1b). XRD analysis (Figure 1c) of the as-received α-SiC sample confirmed that α-SiC is the main phase while TiB_2 and graphite are the minor secondary phases, which is consistent with the SEM analysis.

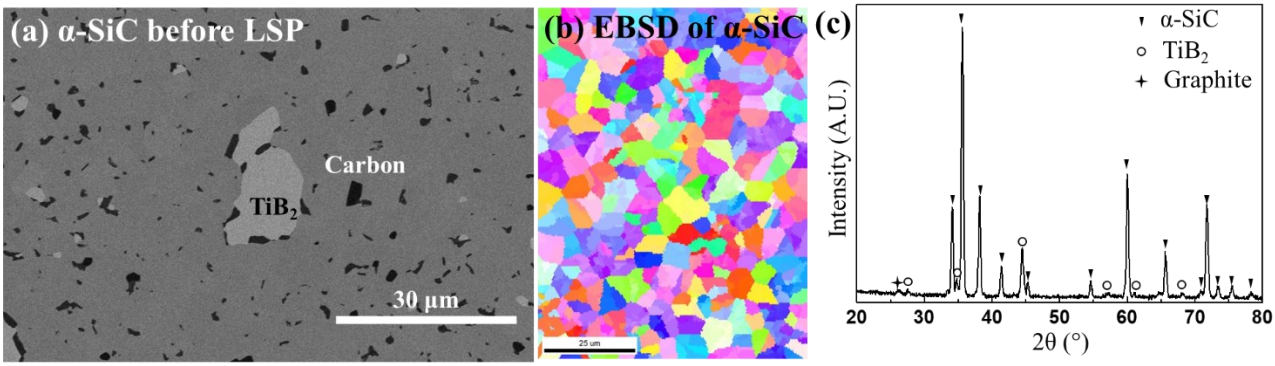

Figure 1. (a) SEM (backscattered electron image), (b)
EBSD inverse pole figure of the grain structure, and (c) XRD of the as-received α-SiC sample.

The HT-LSP experimental setup is shown in **Figure 2** [26]. The α-SiC sample, a sacrificial layer of 50 μm thick stainless-steel 309 (SS309) foil, and a plasma confining media of 3 mm thick fused silica glass were put into a sample holder, which was placed on a 3D stage that can control the sample movement during HT-LSP. The sample was heated to 1000 ℃ in a tube furnace (OTF-1200X, MTI

Corporation, Richmond, CA) in a flowing argon atmosphere. A Q-switched neodymium-doped yttrium aluminum garnet (Nd:YAG) pulse laser (PRII 8010; Continuum Electro-Optics, San Jose, California) with a wavelength of 1064 nm and a pulse duration of 7 ns was used. The laser beam with a pulse energy of 850 mJ was focused to a 1 mm diameter spot. The peak power density was calculated as 15.4 GW/cm^2, below the breakdown threshold of silica glass [29]. The shock wave pressure was calcuated as 15.0 GPa using the analytical model developed by Berthe et al. [30]:

$$P = 0.01\sqrt{\frac{\alpha}{2\alpha+3}}\sqrt{Z}\sqrt{I_0} \quad (1)$$

$$\frac{2}{Z} = \frac{1}{Z_1} + \frac{1}{Z_2} \quad (2)$$

where P is the peak shock wave pressure, α is the fraction of internal energy converted to thermal energy (0.25), Z is the reduced shock impedance between the alumina and plasma confining glass, and I_0 is laser power density. The shock impedancess of silica glass (Z_1) and α-SiC (Z_2) are 1.21×10^7 and 4.2×10^7 Kg/m^{2}s, respectively. In the HT-LSP process, the pulsed laser passed through a transparent fused silica glass and irradiated the sacrificial layer of SS309 foil. The sacrificial layer absorbs the laser energy and forms a plasma. The fast expansion of the plasma generated shock waves, which penetrates into the SiC sample to generate a high compressive residual stress. Although there is a high temperature in the plasma, the SS309 sacrificial layer protected the SiC sample from the laser heating. The temperature increase caused by the laser irradiation is thus negligible, which has been verified by the comparison of LSP of sapphire with and without the furnace heating in our previous work [27]. The temperature of the SiC sample is solely controlled by the furnace temperature (1,000 ºC).

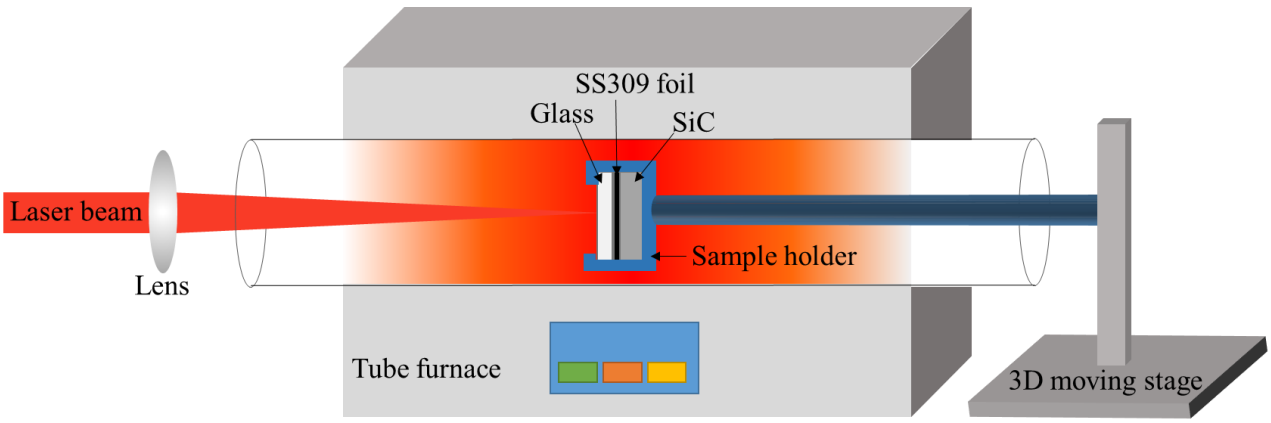

Figure 2. Schematic diagram of the HT-LSP setup of α-SiC ceramics.

The surface morphology of the α-SiC samples before and after HT-LSP were characterized by scanning electron microscopy (SEM, Helios 660, FEI) and a 3D optical profiling system (NewView 8300, Zygo Corporation). The average grain size of α-SiC was measured by the electron backscatter diffraction (EBSD) analysis, which was performed in the Helios 660 equipped with an EBSD detector (Hikari XP 2, AMETEK). Microstructures, including dislocations and stacking faults, were revealed by cross-sectional transmission electron microscopy (TEM, 200kV FEI Talos 200i) using diffraction contrast. TEM samples were extracted from the sample surface near and far from the HT-LSP region by focused ion beam (FIB). The samples were extracted using a FEI Helios 660 FIB and then thinned using a FEI Helios 600 or Helios G4 PFIB CXE. Selected area electron diffraction patterns (SAEDPs) were collected and indexed to determine the crystallographic orientation of grains according to crystallographic information file (CIF) 6H SiC mp-7361 from the Materials Project. Energy dispersive X-ray spectroscopy (EDS; Bruker XFlash 6T30) was used to collect elemental maps in the TEM samples while operating in the scanning mode (S/TEM).

The residual stress distribution in the HT-LSP treated region was measured using a confocal Raman microscope (Renishaw plc, Wotton-under-Edge, UK) equipped with an Argon ion laser with a wavelength of 514.5 nm. The microscope was operated in the backscattering mode with a 20× objective lens. In confocal Raman microscopy, the laser spot size and depth are estimated by:

$$\emptyset \approx \frac{2n\lambda}{\pi NA} \tag{3}$$

$$Z \approx \frac{2.2n\lambda}{\pi NA^2} \tag{4}$$

where *NA* is the numerical aperture of the objective (0.25), λ is the wavelength of the incident light (514.5 nm), and *n* is the refractive index of the sample. The refractive index of α-SiC at 514 nm laser is 2.7[31]. Thus, the calculated laser spot size is 2.3 μm and the depth is 10.3 μm. The laser spot size is smaller than the average grain size of α-SiC (6.4 μm). The resolution of wavenumber in the present measurement is 0.3 cm^{-1} at the full width at half maximum (FWHM). The Raman spectrum of the as-received stress-free α-SiC (verified by measuring the surface stress by XRD) consists of four peaks in the range of 700-1000 cm^{-1} [32]. The peaks in the Raman spectrum were attributed to the phonon lines of α-SiC [33]. The Raman peak at 789.2 cm^{-1} was used to measure the residual stress. When α-SiC is loaded with a stress, the position of the Raman peak is shifted from that in the stress-free material. The

relationship between Raman peak shift and applied stress has been studied by several groups [34–36]. Liu et al. [37] investigated the Raman shift of α-SiC as a function of hydrostatic pressure up to 95 GPa and developed an equation for the relationship between the Raman shift and residual stress:

$$\omega_{TO}(cm^{-1}) = 789.2 + 3.11P - 0.009P^2, \quad (5)$$

where ω_{TO} refers to the peak position of the transverse optical peak, and P is the residual stress in the unit of GPa. $\omega_{TO} = 789.2\ cm^{-1}$ is in the stress-free state. A blue shift of the Raman peak indicates compressive residual stress while a red shift indicates tensile residual stress. Residual stress mapping with a step size of 40 μm was used to present the 2-D distribution of residual stress in the HT-LSP treated spot. The line scan measurement of the residual stress with a step size of 20 μm was used to obtain more accurate values and 1-D distribution of the residual stress. The Raman spectra were recorded with an accumulation time of 10 s. To measure the depth profile of residual stress, the HT-LSP treated SiC was cut to reveal cross-section of HT-LSP spot, and then was polished by a 3 μm diamond lapping film and a 50 nm colloidal silica solution to carefully remove the machining damage. Vickers indentations were applied with an indentation load of 3N and a dwell time of 10 seconds. The apparent plane-strain fracture toughness was measured by the Vickers indentation technique and an equation developed by Anstis et al. [38, 39]:

$$K_{Ic} = 0.016\left(\frac{E}{H}\right)^{1/2}\frac{P}{a^{3/2}}, \quad (6)$$

where E is Young's modulus, H is the Vickers hardness, P is the load, and a is half the total length of the straight cracks. The fracture toughness was calculated from 30 indents in each sample to allow the statistical analysis. The nanohardness of samples was measured by nanoindentation with a Berkovich tip at a load of 8000 μN.

3. Experimental Results and Discussion

3.1 Surface morphology before and after HT-LSP

The surface morphology of the α-SiC sample after HT-LSP is presented in **Figure 3.** The HT-LSP treated spot was 1 mm in diameter and the boundary was marked by a red-dotted circle (Figure 3a). TiO_2 (confirmed by the EDS analysis) and small holes (Figure 3b) were observed in the HT-LSP sample and were likely formed by oxidation of the TiB_2 and carbon impurities at 1000 ℃ by reactions with the residual oxygen in the flowing Ar. TiB_2 was oxidized to TiO_2 after oxidation, while carbon

left the surface when turned into gaseous CO_2, resulting in small holes. These holes and micro-cracks may degrade the fracture strength of the sample, and this issue will be solved by using α-SiC samples without carbon impurity as well as providing more Ar gas to prevent oxidation of samples in future. Fortunately, further TEM analysis suggests that TiO_2 and small holes were present only in the top surface layer (< 3 μm). Other than the pores formed by oxidation, no obvious cracks were found in the HT-LSP treated spot. Occasionally, some localized microcracks were generated (Figure 3c), which may be caused by the pre-existing flaws in the samples and the thermal stress. The thermal expansion coefficients of SiC, TiB_2, TiO_2, and graphite are $4\times10^{-6}K^{-1}$ [40], 7×10^{-6} K^{-1} [41], 8.4×10^{-6} K^{-1} and 4×10^{-6} K^{-1}, respectively, which are close to each other. Thus, the thermal expansion mismatch at the phase interfaces is low and may not cause significant microcracks during the cooling process.

The arithmetic mean height (S_a) of the α-SiC sample before HT-LSP was 4 nm. After heating without HT-LSP, S_a was increased to 11 nm due to surface oxidation at 1000 ºC. After HT-LSP, S_a became 16 nm. These results suggest that the surface roughness of α-SiC was increased after HT-LSP, which is consistent with literatures of LSP at room temperature[6, 19]. However, the majority of surface roughness increase after HT-LSP is attributed to the surface oxidation.

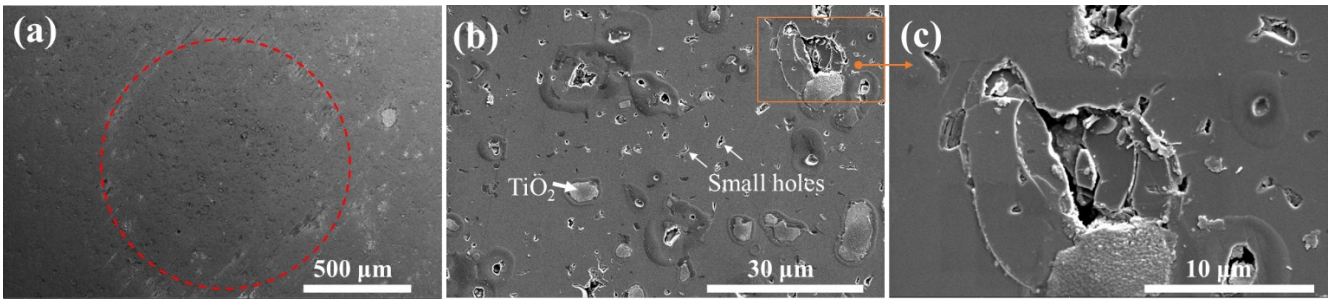

Figure 3. SEM (secondary electron image) of the surface of SiC sample after HT-LSP at 1000 °C: (a) the HT-LSP spot with the boundary indicated by the red dotted circle; (b) TiO_2 and small holes on the surface; (c) enlarged view of a damage region indicated by the orange frame and arrow in b).

3.2 Compressive residual stress in α-SiC after HT-LSP

Raman spectroscopy was used to measure the residual stress distribution in the HT-LSP -treated region. A representative Raman spectrum of the as-received stress-free α-SiC samples is shown in Figure 4a. Four Raman peaks were well resolved, which were attributed to folded phonon modes of different symmetry. The peaks at 768.8 and 789.2 cm^{-1} are assigned to E_2 (tranverse optical, TO) phonon modes.

The peak at 797.4 cm^{-1} is assigned to the E_1(TO) phonon mode. The peak at 970.2 cm^{-1} is attributed to the A_1 (longitudinal optical, LO) mode of α-SiC [42]. The peak of 789.2 cm^{-1} corresponding to the TO phonon mode was used to measure the residual stress. Figure 4b compares the Raman spectrum collected from α-SiC before and after HT-LSP (collected at the center of laser-treated spot), wihch showed a blue peak shift after HT-LSP . The distribution of the residual stress in the HT-LSP treated region is presented in Figures 4c and 4d, which was calculated using Equation 5. The 2-D mapping of the residual stress (Figure 4c) was conducted with a resolution of 40 μm to show the trend of residual stress distribution inside the HT-LSP treated spot (1 mm in diameter), in which the blocks with brighter green contrast represent a higher wavenumber and, thus, a higher magnitude of compressive residual stress. The 1-D Raman line scan used to provide a profile of residual stress (Figure 4d) was performed at a finer resolution (20 μm) to better show the magnitude change of the residual stress across the HT-LSP treated spot. The compressive residual stress reached a maximum of ~650 MPa at the center of the HT-LSP treated spot and decreased away from the center. It was also noted that a tensile residual stress of ~150 MPa was present at the edge of the HT-LSP treated spot, which may have been generated to compensate for the high magnitude of compressive residual stress at the center. The depth profile of the measured compressive residual stress is shown in Fig. 4e, suggesting the compressive residual stress gradually decreases with the depth and reduced to zero at a depth of about 550 μm.

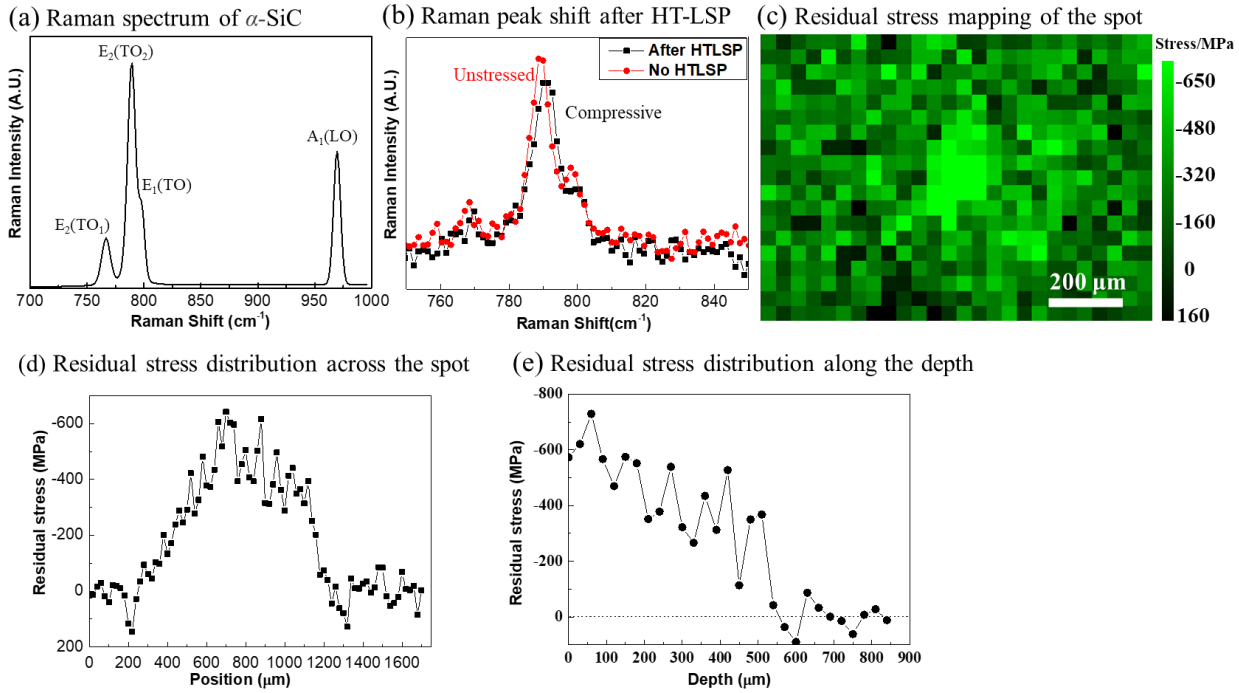

Figure 4. (a) Representative Raman spectrum collected from the α-SiC sample; (b) Raman spectra collected before and after HT-LSP ; (c) mapping of the residual stress distribution after HT-LSP, with brighter blocks representing a higher compressive residual stress; (d) residual stress distribution determined from the line scan taken across the HT-LSP spot; and (e) Residual stress distribution along the depth of HT-LSP treated α-SiC.

3.3 Cross-Section Microstructures before and after HT-LSP

Figure 5a is a bright-field (BF) TEM micrograph of the α-SiC sample far away from the HT-LSP treated region. This control region underwent the same heating process to 1000 ºC but was not exposed to the HT-LSP treatment. Several grains show stacking faults spanning the entire grain width, as indicated by the arrow in Figure 5a. Figure 5b shows a high angle-annular dark field (HAADF) S/TEM image taken from the region outlined with an orange box in Figure 5a, where EDS mapping of C, Si, B, and Ti elements was conducted (Figures 5c-e). These EDS maps reveal that the microstructure of untreated region includes three phases: SiC, a Ti- and B-rich phase (TiB_2), and a carbon phase, which are consistent with the SEM and XRD results of the as-received α-SiC sample (Figure 2). Unlike the surface (Figure 3), the carbon and Ti and B-rich phases, which are approximately 4 μm beneath the surface, did not appear to be oxidized. Sparse oxygen content was detected across the entire EDS area, but was not present in concentrations that would suggest the presence of an oxide.

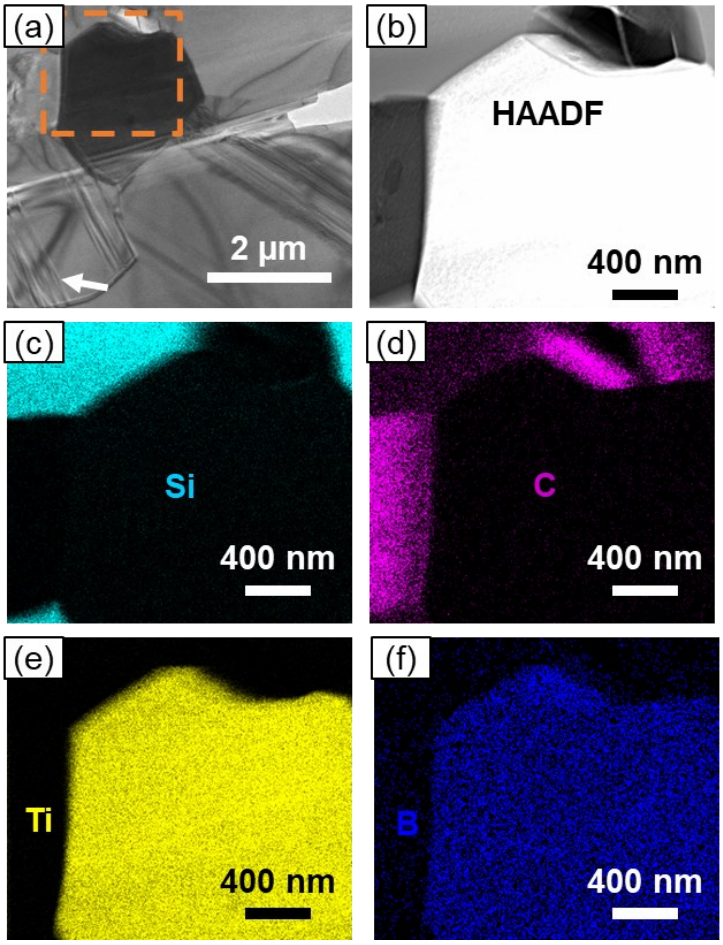

Figure 5: (a) BF-TEM micrograph showing the microstructures of α-SiC without HT-LSP. The white arrow indicates stacking faults. (b) HAADF S/TEM micrograph of the region outlined with orange dashed box in a). (c, d, e,f) Elemental maps of Si, C, Ti, and B respectively, collected with EDS in the region showed in b).

Figure 6 is a BF-TEM micrograph from the HT-LSP treated region. Similar to the region without HT-LSP shown in Figure 5, several grains have stacking faults along the entire width of the grain. However, several grains (*e.g.* Grain A) had a higher density of straight dislocations, which were not observed outside of the HT-LSP region. For example, Figure 6b is a BF-TEM image showing the dislocations in Grain A when tilted to the [$\bar{1}$100] zone axis (see SAEDP in the inset). The dislocations lie on the (0001) plane, which agrees with previous reports that slip of dislocations in α-SiC occurs on the basal plane above 800 ºC [43]. It is important to note that no stacking faults or dislocations were observed in Grain B, which was oriented such that the imaging conditions necessary to observe dislocations on the basal plane were not achievable within the tilt range of the holder.

The plasticity of α-SiC is strongly dependent on the temperature, and its dislocation mobility increases

substantially when the temperature is above 800 ℃ [43, 44]. The critical resolved shear stress of basal plane slip in α-SiC decreases rapidly with increasing temperature and becomes 200 MPa at 1000 ℃ [45]. Carter and Davis suggested that the dislocations on the primary basal slip system $(0001)[11\bar{2}0]$ of α-SiC can be dissociated into Shockley partials [46]. A Knoop indentation study of α-SiC single crystals by Fujita et al. [47] observed the slip traces along $[11\bar{2}0]$ on the basal plane above 800 °C.

On the other hand, α-SiC was subjected to an ultra-high strain rate (10^6-10^8 s^{-1}) dynamic deformation condition due to the very short laser pulses (7 ns) and the high shock wave pressure (15.0 GPa) during the HT-LSP process [48]. In addition, the α-SiC samples contain the heterogeneous microstructures with the impurity of TiB_2 and graphite. The shock wave incident on the interface (e.g., SiC/TiB_2) is partially back-reflected and partially transmitted, the percentage of which depends on the acoustic impedance of the two phases[49]. An enhancement of shock wave pressure can occur at the interface due to the acoustic impedance mismatch of the two phases [50]. The shock wave pressure of 15 GPa or above is in the range of the Hugoniot elastic limit (HEL) of α-SiC reported in the literature. HEL is a transition point at which the response of ceramics to a shock loading transfers from the elastic to inelastic deformation [51]. While HEL of α-SiC depends on the microstructural features such as grain size, porosity and impurities, its value ranges from 8 to 19 GPa [52–54]. Kobayashi et al. reported that the inelastic deformation of α-SiC starts to occur between 10 and 30 GPa, and is fully developed when the shock loading is above 30 GPa [54, 55]. Therefore, the combination of a high shock pressure (15 GPa) and a lower critical resolved shear stress of α-SiC at 1000 ℃ (200 MPa) may result in the dislocation slip in α-SiC ceramics during the HT-LSP process, which may further generate the localized plastic deformation and compressive residual stress.

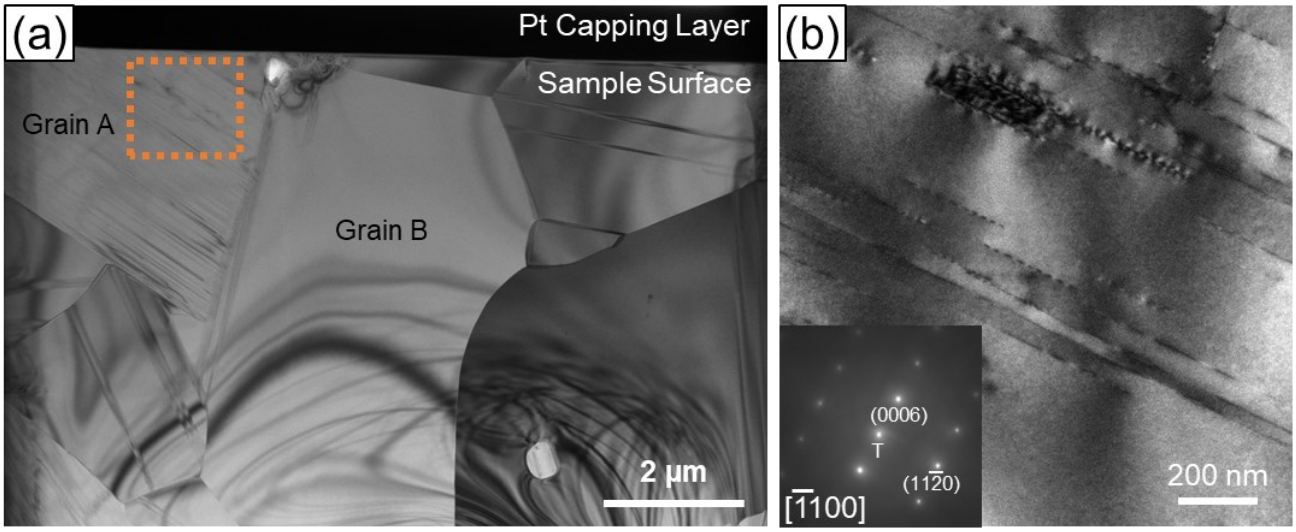

Figure 6: (a) BF-TEM micrograph of α-SiC sample exposed to HT-LSP. (b) BF-TEM image from Grain A when tilted to the $[\bar{1}100]$ zone axis; (inset) the indexed SAEDP.

3.4 Cracking Resistance after HT-LSP

The cracking resistance of α-SiC before and after HT-LSP was evaluated by the Vickers indentation method to study the influence of local compressive residual stress on the crack propagation on the surface. **Figure 7** shows the representative SEM images of Vickers indentations on the regions with and without a HT-LSP treatment, respectively. There was no significant change in the Vickers hardness of α-SiC after HT-LSP. The Vickers hardness of α-SiC before and after HT-LSP was 26.0±1.4 and 25.4 ± 2.0 GPa, respectively. The nanoindentation hardness of α-SiC before and after HT-LSP treatment was 40.1±1.2 GPa and 43.4±1.9 GPa, respectively. The nanoindentation hardness increase (~8%) could be attributed to the compressive residual stress induced by HT-LSP, which can reduce the shear stresses produced by the compressive force of the indenter, resulting in a smaller indent size and higher hardness.[56]

Compared with the sample without HT-LSP, the average radius of the radial cracks after HT-LSP was reduced by 24% from 34 to 26 μm. The in-plane fracture toughness of α-SiC was increased by 36% from 2.5±0.15 to 3.4±0.20 $MPam^{1/2}$ after HT-LSP, which was calculated using Equation 4. This indicates that the resistance to crack propagation on the surface of α-SiC has been significantly improved by the HT-LSP treatment. Because HT-LSP is a surface treatment, the in-plane fracture toughness measured by the indentation methods may better represent the improvement of the local mechanical properties near the surface of α-SiC by HT-LSP, rather than the macroscale methods such

as the single-edged notch beam (SENB) method.

Compressive residual stress was found to be beneficial to the cracking resistance of several ceramic materials such as α-Al_2O_3[7, 18] and α-SiC[16, 25] after LSP at room temperature, as well as sapphire after HT-LSP[27]. The stress intensity factor of a straight crack under a uniform compressive residual stress is reduced to [57]:

$$K_I = {}^0K_I - 2\left(\frac{c}{\pi}\right)^{1/2} \int_0^w \frac{\sigma_0}{\sqrt{(c^2-x^2)}} dx \quad (7)$$

where K_I is the stress intensity with the compressive residual stress, ${}^0K_I$ is the original stress intensity without the residual stress, c is the Griffith flaw size, and w is the thickness of the residual stress layer. According to Equation 5, a compressive residual stress as high as 650 MPa on SiC surface may reduce the stress intensity factor at the crack tip and, thus, retard the crack propagation[58].

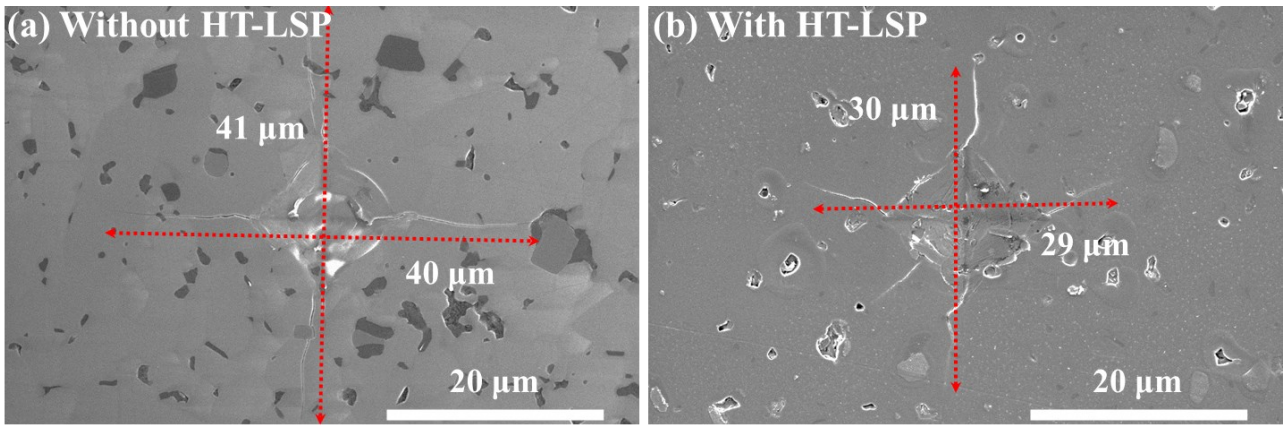

Figure 7. Comparison of the radial cracks on the edge of Vickers indentation in the (a) untreated and (b) HT-LSP treated α-SiC sample.

4. Conclusions

The influence of the HT-LSP process on the compressive residual stress and mechanical response of polycrystalline α-SiC was investigated. After HT-LSP at 1000 °C, the surface of α-SiC exhibited few microcracks and slight oxidation of TiB_2 and graphite impurities. The residual stress distribution was measured using Raman spectroscopy, which showed that a high compressive residual stress up to 650 MPa was introduced into the surface of α-SiC by HT-LSP. TEM characterizations revealed dislocation slips on the basal planes, suggesting that plastic deformation occurred in α-SiC during the HT-LSP

process that may be caused by the combination of a high shock pressure and a lower critical resolved shear stress at 1000 ℃. As a result of the compressive residual stress, the nanohardness and in-plane fracture toughness of α-SiC was increased by 8% and 36%, respectively. These experimental results suggest that HT-LSP is a promising technique to overcome the technical challenges associated with the traditional LSP process at room temperature by enhancing the plasticity of ceramic materials and suppressing microcrack formation to improve the mechanical properties.

Acknowledgements

This material is based upon work supported by the National Science Foundation under Grant No. 2023404. The research was performed in part in the Nebraska Nanoscale Facility: National Nanotechnology Coordinated Infrastructure and the Nebraska Center for Materials and Nanoscience (and/or NERCF), which are supported by the National Science Foundation under Award ECCS: 2025298, and the Nebraska Research Initiative.

References

1. Hornberger J, Lostetter AB, Olejniczak KJ, McNutt T, Lal SM, Mantooth A. Silicon-carbide (SiC) semiconductor power electronics for extreme high-temperature environments. *2004 IEEE Aerosp. Conf. Proc. IEEE Cat No04TH8720*. Vol. 4. 2004:2538-2555 Vol.4. https://doi.org/10.1109/AERO.2004.1368048
2. Naslain R, Christin F. SiC-Matrix Composite Materials for Advanced Jet Engines. *MRS Bull*. 2003;28(9):654–658. https://doi.org/10.1557/mrs2003.193
3. Jang GH, Cho KH, Park SB, Lee WG, Hong US, Jang H. Tribological properties of C/C-SiC composites for brake discs. *Met Mater Int*. 2010;16(1):61–66. https://doi.org/10.1007/s12540-010-0061-4
4. Kaur S, Cutler RA, Shetty DK. Short-Crack Fracture Toughness of Silicon Carbide. *J Am Ceram Soc*. 2009;92(1):179–185. https://doi.org/10.1111/j.1551-2916.2008.02829.x
5. Sano Y, Obata M, Kubo T, *et al.* Retardation of crack initiation and growth in austenitic stainless steels by laser peening without protective coating. *Mater Sci Eng A*. 2006;417(1):334–340. https://doi.org/10.1016/j.msea.2005.11.017
6. Shukla PP, Swanson PT, Page CJ. Laser shock peening and mechanical shot peening processes applicable for the surface treatment of technical grade ceramics: a review. *Proc Inst Mech Eng Part B J Eng Manuf*. 2014;228(5):639–652.
7. Wang F, Zhang C, Lu Y, Nastasi M, Cui B. Laser shock processing of polycrystalline alumina

ceramics. *J Am Ceram Soc*. 2017;100(3):911–919.
8. R S, P G, Gupta RK, *et al.* Laser Shock Peening and its Applications: A Review. *Lasers Manuf Mater Process*. 2019;6(4):424–463. https://doi.org/10.1007/s40516-019-00098-8
9. Kumagai M, Curd ME, Soyama H, Ungár T, Ribárik G, Withers PJ. Depth-profiling of residual stress and microstructure for austenitic stainless steel surface treated by cavitation, shot and laser peening. *Mater Sci Eng A*. 2021;813:141037. https://doi.org/10.1016/j.msea.2021.141037
10. Zhang C, Dong Y, Ye C. Recent Developments and Novel Applications of Laser Shock Peening: A Review. *Adv Eng Mater*. n.d.;n/a(n/a):2001216. https://doi.org/10.1002/adem.202001216
11. Lu Q, Su Q, Wang F, *et al.* Influence of laser shock peening on irradiation defects in austenitic stainless steels. *J Nucl Mater*. 2017;489:203–210.
12. Yan X, Wang F, Deng L, *et al.* Effect of laser shock peening on the microstructures and properties of oxide-dispersion-strengthened austenitic steels. *Adv Eng Mater*. 2018;20(3):1700641.
13. Lu JZ, Luo KY, Yang DK, *et al.* Effects of laser peening on stress corrosion cracking (SCC) of ANSI 304 austenitic stainless steel. *Corros Sci*. 2012;60:145–152.
14. Luong H, Hill MR. The effects of laser peening and shot peening on high cycle fatigue in 7050-T7451 aluminum alloy. *Mater Sci Eng A*. 2010;527(3):699–707.
15. Montross CS, Wei T, Ye L, Clark G, Mai Y-W. Laser shock processing and its effects on microstructure and properties of metal alloys: a review. *Int J Fatigue*. 2002;24(10):1021–1036.
16. Shukla P, Nath S, Wang G, Shen X, Lawrence J. Surface property modifications of silicon carbide ceramic following laser shock peening. *J Eur Ceram Soc*. 2017;37(9):3027–3038. https://doi.org/10.1016/j.jeurceramsoc.2017.03.005
17. Wang F, Yan X, Zhang C, *et al.* Localized plasticity in silicon carbide ceramics induced by laser shock processing. *Materialia*. 2019;6:100265. https://doi.org/10.1016/j.mtla.2019.100265
18. Shukla P, Crookes R, Wu H. Shock-wave induced compressive stress on alumina ceramics by laser peening. *Mater Des*. 2019;167:107626.
19. Akita K, Sano Y, Takahashi K, Tanaka H, Ohya SI. Strengthening of Si3N4 ceramics by laser peening. *Mater. Sci. Forum*. Vol. 524. Trans Tech Publ; 2006:141–146.
20. Sundar R, Ganesh P, Gupta RK, *et al.* Laser shock peening and its applications: a review. *Lasers Manuf Mater Process*. 2019;6(4):424–463.
21. Yella P, Venkateswarlu P, Buddu RK, *et al.* Laser shock peening studies on SS316LN plate with various sacrificial layers. *Appl Surf Sci*. 2018;435:271–280.
22. Zhang D, Wu L-C, Ueki M, Ito Y, Sugioka K. Femtosecond laser shockwave peening ablation in liquids for hierarchical micro/nanostructuring of brittle silicon and its biological application. *Int J Extreme Manuf*. 2020;2(4):045001. https://doi.org/10.1088/2631-7990/abb5f3
23. Wang F, Zhang C, Yan X, *et al.* Microstructure-property relation in alumina ceramics during post-annealing process after laser shock processing. *J Am Ceram Soc*. 2018;101(11):4933–4941.
24. Kiani S, Leung KWK, Radmilovic V, *et al.* Dislocation glide-controlled room-temperature plasticity in 6H-SiC single crystals. *Acta Mater*. 2014;80:400–406. https://doi.org/10.1016/j.actamat.2014.07.066
25. Localized plasticity in silicon carbide ceramics induced by laser shock processing - ScienceDirect. n.d.
26. Cui B, Wang F, Lu Y, Nastasi M. Systems for and methods for improving mechanical properties of ceramic material. 2020.
27. Wang F, Yan X, Liu L, Nastasi M, Lu Y, Cui B. Surface strengthening of single-crystal alumina

by high-temperature laser shock peening. *Mater Res Lett*. 2021;9(3):155–161. https://doi.org/10.1080/21663831.2020.1862933
28. Pak AY, Rudmin MA, Mamontov GY, Bolotnikova OA. Electroarc synthesis and cleaning from carbon impurities of cubic silicon carbide in the air atmosphere. *J Superhard Mater*. 2018;40(3):157–163.
29. Sharma BS, Rieckhoff KE. Laser-induced dielectric breakdown and mechanical damage in silicate glasses. *Can J Phys*. 1970;48(10):1178–1191. https://doi.org/10.1139/p70-149
30. Fabbro R, Fournier J, Ballard P, Devaux D, Virmont J. Physical study of laser-produced plasma in confined geometry. *J Appl Phys*. 1990;68(2):775–784.
31. Choyke WJ, Patrick L. Refractive Index and Low-Frequency Dielectric Constant of 6H SiC. *JOSA*. 1968;58(3):377–379. https://doi.org/10.1364/JOSA.58.000377
32. Feldman DW, Parker JH, Choyke WJ, Patrick L. Raman Scattering in 6H SiC. *Phys Rev*. 1968;170(3):698–704. https://doi.org/10.1103/PhysRev.170.698
33. Nakashima S -i, Harima H. Raman investigation of SiC polytypes. *Phys Status Solidi A*. 1997;162(1):39–64.
34. Gigler AM, Huber AJ, Bauer M, Ziegler A, Hillenbrand R, Stark RW. Nanoscale residual stress-field mapping around nanoindents in SiC by IR s-SNOM and confocal Raman microscopy. *Opt Express*. 2009;17(25):22351–22357. https://doi.org/10.1364/OE.17.022351
35. Watts J, Hilmas G, Fahrenholtz WG, Brown D, Clausen B. Stress measurements in ZrB2–SiC composites using Raman spectroscopy and neutron diffraction. *J Eur Ceram Soc*. 2010;30(11):2165–2171. https://doi.org/10.1016/j.jeurceramsoc.2010.02.014
36. DiGregorio JF, Furtak TE. Analysis of Residual Stress in 6H-SiC Particles within Al2O3/SiC Composites through Raman Spectroscopy. *J Am Ceram Soc*. 1992;75(7):1854–1857. https://doi.org/10.1111/j.1151-2916.1992.tb07207.x
37. Liu J, Vohra YK. Raman modes of 6 h polytype of silicon carbide to ultrahigh pressures: A comparison with silicon and diamond. *Phys Rev Lett*. 1994;72(26):4105.
38. Anstis GR, Chantikul P, Lawn BR, Marshall DB. A Critical Evaluation of Indentation Techniques for Measuring Fracture Toughness: I, Direct Crack Measurements. *J Am Ceram Soc*. 1981;64(9):533–538. https://doi.org/10.1111/j.1151-2916.1981.tb10320.x
39. Evans AG, Charles EA. Fracture Toughness Determinations by Indentation. *J Am Ceram Soc*. 1976;59(7–8):371–372. https://doi.org/10.1111/j.1151-2916.1976.tb10991.x
40. Chua BW, Lu L, Lai MO. Influence of SiC particles on mechanical properties of Mg based composite. *Compos Struct*. 1999;47(1):595–601. https://doi.org/10.1016/S0263-8223(00)00031-3
41. Wang J, McDannald A, Karandikar P, Aghajanian M. Fabrication of reaction bonded TiB2/Si/SiC composites for thermal applications. *Int J Ceram Eng Sci*. 2020;2(5):264–270. https://doi.org/10.1002/ces2.10067
42. Aksyanov IG, Kompan ME, Kul'kova IV. Raman scattering in mosaic silicon carbide films. *Phys Solid State*. 2010;52(9):1850–1854. https://doi.org/10.1134/S1063783410090106
43. Niihara K. Slip systems and plastic deformation of silicon carbide single crystals at high temperatures. *J Common Met*. 1979;65(1):155–166. https://doi.org/10.1016/0022-5088(79)90161-9
44. Maeda K, Suzuki K, Fujita S, Ichihara M, Hyodo S. Defects in plastically deformed 6H SiC single crystals studied by transmission electron microscopy. *Philos Mag A*. 1988;57(4):573–592.

https://doi.org/10.1080/01418618808214408
45. Fujita S, Maeda K, Hyodo S. Dislocation glide motion in 6H SiC single crystals subjected to high-temperature deformation. *Philos Mag A*. 1987;55(2):203–215. https://doi.org/10.1080/01418618708209845
46. Carter CH, Davis RF, Bentley J. Kinetics and Mechanisms of High-Temperature Creep in Silicon Carbide: I, Reaction-Bonded. *J Am Ceram Soc*. 1984;67(6):409–417. https://doi.org/10.1111/j.1151-2916.1984.tb19726.x
47. Fujita S, Maeda K, Hyodo S. Anisotropy of high-temperature hardness in 6H silicon carbide. *J Mater Sci Lett*. 1986;5(4):450–452. https://doi.org/10.1007/BF01672358
48. Braisted W, Brockman R. Finite element simulation of laser shock peening. *Int J Fatigue*. 1999;21(7):719–724. https://doi.org/10.1016/S0142-1123(99)00035-3
49. Salzmann D, Eliezer S, Krumbein AD, Gitter L. Laser-driven shock-wave propagation in pure and layered targets. *Phys Rev A*. 1983;28(3):1738–1751. https://doi.org/10.1103/PhysRevA.28.1738
50. Cottet F, Hallouin M, Romain JP, Fabbro R, Faral B, Pepin H. Enhancement of a laser-driven shock wave up to 10 TPa by the impedance-match technique. *Appl Phys Lett*. 1985;47(7):678–680. https://doi.org/10.1063/1.96055
51. Grady DE. Shock-wave compression of brittle solids. *Mech Mater*. 1998;29(3–4):181–203.
52. Sekine T, Kobayashi T. Shock compression of 6H polytype SiC to 160 GPa. *Phys Rev B*. 1997;55(13):8034–8037. https://doi.org/10.1103/PhysRevB.55.8034
53. Bourne N, Millett J, Pickup I. Delayed failure in shocked silicon carbide. *J Appl Phys*. 1997;81(9):6019–6023. https://doi.org/10.1063/1.364450
54. Grady DE, Kipp ME. Sandia Report No. *SAND92-1832 Sandia Natl Lab Albuq NM*. 1993.
55. Kobayashi T, Sekine T, He H. Effect of Inelastic Deformation on Crystallite Size in Post-Shock 6H Polytype SiC. *Phys Rev Lett*. 2000;85(14):2969–2972. https://doi.org/10.1103/PhysRevLett.85.2969
56. Huang Y-C, Chang S-Y, Chang C-H. Effect of residual stresses on mechanical properties and interface adhesion strength of SiN thin films. *Thin Solid Films*. 2009;517(17):4857–4861. https://doi.org/10.1016/j.tsf.2009.03.043
57. Lawn BR. Fracture of brittle solids. *Camb Solid State Sci Ser*. 1993.
58. Green DJ. Compressive surface strengthening of brittle materials by a residual stress distribution. *J Am Ceram Soc*. 1983;66(11):807–810.